Chapitre 2

Performance Optimization of a Multi-DoF Bilateral Robot Force Amplification

Résumé

Cet article présente une nouvelle approche afin de déterminer la commande optimale pour un manipulateur robotisé à plusieurs degrés de liberté (multi-ddl) dans un contexte d'amplification de force et d'interaction bilatérale. Le problème principal lors de l'utilisation d'un manipulateur multi-ddls est le lien direct entre sa configuration et sa dynamique. Cette variation de la dynamique du robot est donc prise en compte lors du processus d'optimisation. Ceci permet d'obtenir un contrôleur stable et des performances exceptionnellement élevées. De plus, la stabilité couplée du manipulateur est évaluée en utilisant une version étendue de la stabilité complémentaire qui permet d'éviter les conditions de passivité. Même si l'optimisation proposée ici est basée sur trois indices de performance spécifiques aux amplifications bilatérales, elle peut être aisément adaptée à n'importe quel type d'interactions bilatérales. La stabilité et la performance résultante de la commande optimale sont démontrées pour un manipulateur sériel à sept degrés de liberté avec des tests d'impact sur différentes surfaces de contact.

2.1 Introduction

In recent decades, bilateral robot interaction has been widely covered in the literature. The emergence of teleoperation in the medical field for assistance in treatment or surgery has greatly contributed to this research effort. Indeed, safety and performance are more than crucial for medical applications. Unfortunately, the control strategy used in most robotic systems is often designed for a single degree of freedom (dof) which is far from the current reality in teleoperation where the interaction usually occurs at the end-effector of a multi-dof manipulator. Moreover, during the design phase, the performance is limited by the constraints

on the prevalent stability analysis, which therefore ends up being evaluated solely online, resulting in suboptimal controllers.

This common coupled stability analysis is known as Llewellyn's absolute stability criterion (Llewellyn [1952]) and involves the notion of passivity (Wyatt et al. [1981]). It has been proven that a passive controlled manipulator interacting with passive environments results in a stable interaction (Colgate [1994], Lawrence [1993]). This notion is convenient due to its simplicity but it is rather conservative. Through the years, different methods to relax this conservative condition have emerged. For instance, Hashtrudi-Zaad and Salcudean [2001] and Lamy et al. [2010] proposed to limit the impedance of the operator or the environment to a maximum value which may then be absorbed in the port network for a more accurate stability analysis. Another interesting approach, presented in Haddadi and Hashtrudi-Zaad [2010], makes use of the scattering parameters and wave variables to transform the system impedances into reflection coefficients, and then studies the coupled stability boundaries in the scattering domain. However, the resulting graphical representation provides a visual aid rather than a design tool. Similarly, Jazayeri and Tavakoli [2012] proposed to use the Möbius transformation on Llewellyn's conditions in order to visualize and interpret the boundaries on the interacting impedances allowing at the same time non-passive environment or operator.

To avoid the passivity conditions, robust stability theory has been explored. Early studies were presented in Yan and Salcudean [1996] using the infinity-norm $\mathcal{H}_\infty$ approach, and in Colgate [1993] using the structured singular value analysis for bilateral systems. Recently, the parameter-space approach with environment uncertainties has been proposed in Peer and Buss [2008]. However, the structured singular value analysis remains the state of the art in robust stability analysis. It has been used with modern tools by Buerger for unilateral interactions in Buerger and Hogan [2007] where it has been renamed complementary stability. All the above contributions have been developed for single-dof models. However, Llewellyn's criterion has been extended to multi-dof and multi-lateral systems in Li et al. [2014].

It is important to mention that typical compensator structures for unilateral interactions are often simple and still achieve great performances. It would therefore be interesting to study the possibility to keep these same structures as well for amplification interactions and be able to reach this high level of performance.

In this chapter, complementary stability is extended to a multi-dof bilateral system. An algorithm that computes the optimal parameter values for pre-defined controller structures for all possible manipulator configurations is presented. Section 2.2 presents an overview of the optimization process. Section 2.3 recalls the notion of port-interaction. Then, robust stability analysis for a multi-dof bilateral device is presented in Section 2.4, followed, in Section 2.5, by the details on the three performance indices selected for the optimization algorithm as well as a controller comparison. Section 2.6 then introduces the manipulator configuration-related

variable that allows to obtain the optimal control law, and discusses some impact test results that assess the performance of the optimization. Finally, a conclusion is drawn in the last section.

2.2 Optimization Process Overview

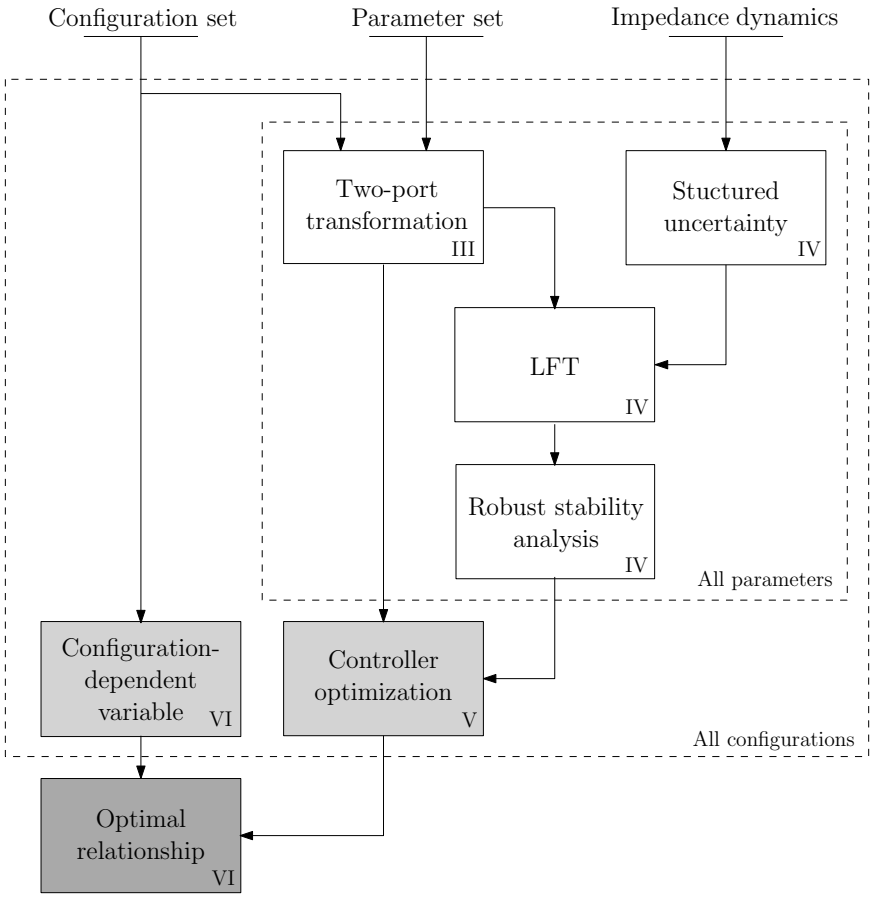

FIGURE 2.1 – General framework of the controller optimization process. The section number associated with each step of this process in the chapter is also given.

The optimization algorithm presented in this chapter includes various notions derived from control theory and from the mechanics of robotic manipulators. It is thus necessary to first introduce the general framework of the algorithm in order to clearly understand the purpose of each step of the optimization process. These steps are shown in Fig 2.1. In short, it is desired to find the optimal parameters for a pre-defined controller structure, a specific robot architecture, and known external interaction inputs. However, the dynamics of a robotic manipulator is usually configuration dependent. It is therefore necessary to determine the optimal control parameters of the *Parameter set* for each configuration from the *Configuration set* in order to keep this optimality at all times. The first step is to rearrange the system

into a two-port interaction in order to isolate the two external input dynamics, namely, the human and environment impedances. These two dynamics, *Impedance dynamics*, have a range of uncertainty and can thus be defined as a *Structured uncertainty* in order to easily recast the system into a linear fractional transformation (LFT). This transformation is convenient to assess the robust stability of the system (*Robust stability analysis*). Then, knowing which parameter values are stable and unstable, the optimization can be performed following certain criteria (*Controller optimization*) which use the dynamics of the controlled manipulator without the dynamics of the external inputs. Finally, each configuration is converted to a unique variable (*Configuration-dependent variable*) that is directly dependent on the manipulator's configuration and that is associated to the optimal control parameters previously found in order to establish the *Optimal relationship*.

2.3 Multi-DoF Two-Port Interaction

The notion of port network has proven through the years to be the most suitable way to analyse systems interactions. It is indeed widely used in motion-force interaction, especially when human beings are in the loop. This notion is briefly recalled here for a two-port interaction, as depicted in Fig. 2.2. Typically, the systems interacting with one another, and their dynamics, are connected through port variables, usually represented by force and velocity. This allows the multiple dynamics to be expressed in terms of mechanical impedances linking them together with the interaction variables. In the case of a bilateral robot interaction, the human and environment impedance matrices are thus described as follows

$$F_o = \mathbf{Z}_o V_o, \tag{2.1}$$

$$F_e = \mathbf{Z}_e V_e \tag{2.2}$$

where $\mathbf{Z}_o$, F_o, V_o, and $\mathbf{Z}_e$, F_e, and V_e are respectively, the human and environment impedance matrices, force vectors and velocity vectors. The rest of the systems is included in the two-port dynamics that usually contains the robot (or the two robots in the case of teleoperation), the communication channels, and the control loops (see Appendix 2.9.1 for details). The link between the forces and velocities is given here by a matrix of admittances and yields

$$\begin{bmatrix} V_o \\ V_e \end{bmatrix} = \begin{bmatrix} \mathbf{Y}_{oo} & \mathbf{Y}_{oe} \\ \mathbf{Y}_{eo} & \mathbf{Y}_{ee} \end{bmatrix} \begin{bmatrix} F_o \\ -F_e \end{bmatrix} = \mathbf{Y} \begin{bmatrix} F_o \\ -F_e \end{bmatrix} \tag{2.3}$$

where $\mathbf{Y}$ is a two-port matrix whose components relate the operator or environment velocities to both the operator and environment forces. The performance optimization presented in this chapter may be applied to any bilateral system. However, the analysis has been developed for a single seven-dof manipulator on which both external forces, namely the operator and the environment interactions, are directly exerted on the structure. The non-collocation of the sensors implies that different velocities must be considered for each external impedance,

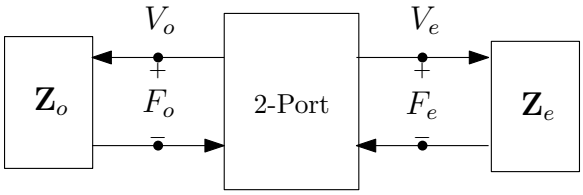

FIGURE 2.2 – Generalized two-port interaction.

which are however related to the same robot joint velocities output with different Jacobian matrices. The redundant nature of the seven-dof manipulator also introduces the need to have a proper redundancy resolution scheme to develop the analysis in the Cartesian space. Here, the Moore-Penrose pseudoinverse of the Jacobian has been used to resolve the redundancy at the centre of the spherical joint (intersection of the last three joint axes). This point is chosen in order to decouple the rotations between the end-effector and the human interaction handle on the fourth link (see Fig. 2.6). A simplified schematic of the system is shown in Fig. 2.3 where $\mathbf{R}$ refers to the redundancy resolution scheme which includes an integrator. $\mathbf{G}_o$ and $\mathbf{G}_e$ are, respectively, the operator and environment regulators while $\mathbf{J}_o$ and $\mathbf{J}_e$ are, respectively, the Jacobian matrices relating the robot joint velocities to the operator and environment velocities. This simplified architecture allows one to easily compute the two-port interaction matrix and then to use the many tools available for stability analysis (details in Appendix 2.9.1).

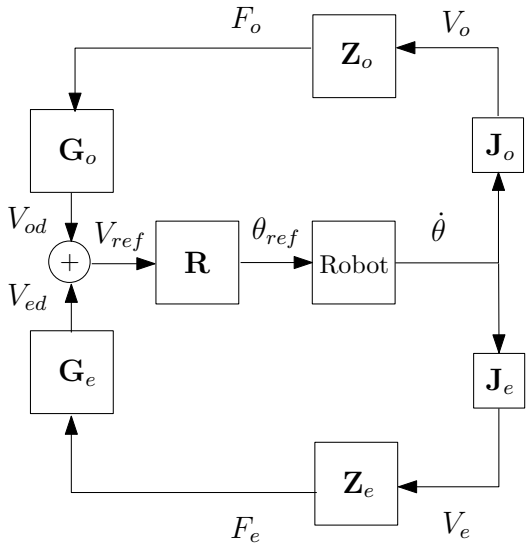

FIGURE 2.3 – Simplified block diagram of the bilateral interaction.

2.4 Stability Analysis

As previously mentioned, many issues still remain open with commonly used stability analyses for bilateral interaction, the most important being the conservative nature of these techniques that unnecessarily restrains performance. Indeed, coupled stability is often validated using the concept of passivity, which has already been extensively covered (Colgate [1994]). Although some techniques can be used to relax the passivity condition using the knowledge of certain components of the interacting dynamics (Hashtrudi-Zaad and Salcudean [2001], Lamy et al. [2010], Haddadi and Hashtrudi-Zaad [2010]), the notion of passivity still limits the manipulator design to a specific set of controllers.

2.4.1 Complementary Stability

The complementary stability proposed in Buerger and Hogan [2007] makes use of the robust analysis tools in order to overcome the requirements for passivity. More specifically, it involves a particular case of the small-gain theorem called structured singular value (Packard and Doyle [1993]) that has further matured into μ-analysis theory. Actually, μ-analysis may be seen as conservative from the point of view of servo design that generally implies well-known dynamics. However, for an interaction system where the operator and environment may be represented by a wide range of different dynamics, this stability analysis is more than relevant. Indeed, the human and environment impedances may be defined as uncertain while keeping them bounded for a known range of application. The analysis thus ensures the coupled stability of the system for specific dynamics (see Appendix 2.9.2 for solutions to robust stability computational issues).

Therefore, this promising technique, previously developed for a unilateral interaction, is extended here to a bilateral interaction. It is important to note that the multi-dof architecture of the manipulator is considered in the computation of each component of the two-port mapping function, $\mathbf{Y}$, using the Jacobian transformation. This two-port mapping function $\mathbf{Y}$ is therefore defined in the Cartesian space as a $[12 \times 12]$ matrix. However, for the robust stability analysis and for the performance optimization described in Section 2.5, only the Cartesian translations are studied and each of these components is evaluated individually. At this stage, the assumption that all Cartesian translational components are *pseudo*-decoupled is possible mainly because the study is on the control of Cartesian amplification, and that, for this reason no major Cartesian motion coupling arises. It also permits to reduce the μ-analysis computation time as well as to optimize the performance related to the different robot configurations as further demonstrated in Section 2.6. Thereby, the two-port mapping function becomes a $[2 \times 2]$ matrix and is denoted $\mathbf{Y}_x$ in the unstructured closed-loop perturbed system represented in Fig. 2.4. The uncertain human and environment dynamics may be defined with additive uncertainties as follows

$$\mathbf{Z}_o(s) = \mathbf{Z}_{on}(s) + \mathbf{W}_o(s)\mathbf{\Delta}_o(s), \tag{2.4}$$

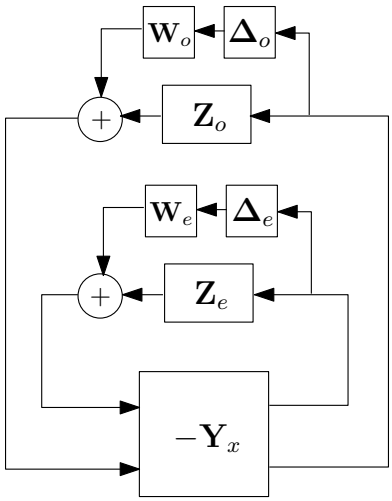

FIGURE 2.4 – Interconnection of one of the robot's Cartesian dof with the operator and environment impedances including additive uncertainties.

$$\mathbf{Z}_e(s) = \mathbf{Z}_{en}(s) + \mathbf{W}_e(s)\mathbf{\Delta}_e(s) \tag{2.5}$$

where $\mathbf{Z}_{on}(s)$ and $\mathbf{Z}_{en}(s)$ are the nominal impedances dynamics, $\mathbf{W}_o(s)$ and $\mathbf{W}_e(s)$ are stable rational weighting functions that define the uncertainty bounds on the operator and environment impedances, $\mathbf{\Delta}_o(s)$ and $\mathbf{\Delta}_e(s)$ are the normalized perturbations, and s is the Laplace variable. The feedback system of Fig. 2.4 is then recast into the convenient linear fractional transformation (LFT) framework with structured uncertainty presented on the left-hand side of Fig. 2.5. Any kind of uncertainty can be represented in this interconnection form and would always generate the same robust stability conditions. Considering the operator and environ-

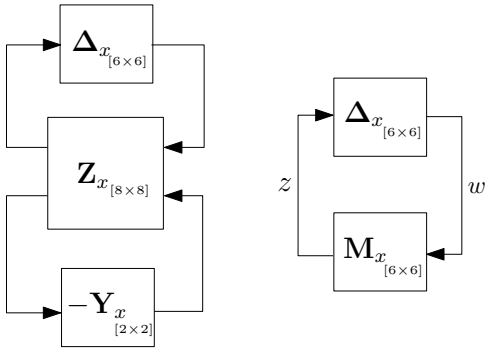

FIGURE 2.5 – LFT form of a single cartesian-dof with the structured uncertainty and its equivalent standard feedback interconnection $\mathbf{M}_x - \mathbf{\Delta}_x$.

ment mechanical impedances as two second-order models, the general impedance form can be described as

$$Z(s) = ms^2 + cs + k \tag{2.6}$$

where m, c, and k are, respectively, the equivalent inertia, damping, and stiffness of the external interactions. To evaluate the coupled stability of the desired dynamics range, uncertainties are added to each impedance parameter, which yields

$$\begin{aligned} m_o &= m_{on} + m_{od}\Delta_{m_o}, \\ c_o &= c_{on} + c_{od}\Delta_{c_o}, \\ k_o &= k_{on} + k_{od}\Delta_{k_o}, \end{aligned} \tag{2.7}$$

$$\begin{aligned} m_e &= m_{en} + m_{ed}\Delta_{m_e}, \\ c_e &= c_{en} + c_{ed}\Delta_{c_e}, \\ k_e &= k_{en} + k_{ed}\Delta_{k_e} \end{aligned} \tag{2.8}$$

where the index n refers to the nominal value of each particular parameter, and the index d refers to the maximum scalar deviation from that value. As previously stated, each Δ represents the normalized uncertainty of each impedance parameter. These six normalized uncertainties may be rewritten as the structured perturbation $\mathbf{\Delta}_x$ of Fig. 2.5, such that

$$\mathbf{\Delta}_x = diag\{\Delta_{m_o}, \Delta_{c_o}, \Delta_{k_o}, \Delta_{m_e}, \Delta_{c_e}, \Delta_{k_e}\} \tag{2.9}$$

and where the uncertainty block structure is defined as follows

$$\mathbf{\Gamma} := \{\mathbf{\Delta}_x : \Delta_i \in \mathbb{R}\} \ , \ i = \{m_o, c_o, k_o, m_e, c_e, k_e\}. \tag{2.10}$$

With this formulation, it is now easy to define the necessary and sufficient condition for robust stability, which is that the inverse of the structured singular value upper bound of the lower LFT, $\mathcal{F}_L[\mathbf{Z}_x, \mathbf{Y}_x]$, noted $\mathbf{M}_x$, is larger than or equal to 1, i.e,

$$[\sup_{\omega\in\mathbb{R}} \mu_{\mathbf{\Gamma}}(\mathbf{M}_x)]^{-1} = [\sup_{\omega\in\mathbb{R}} \mu_{\mathbf{\Gamma}}\{\mathcal{F}_L[\mathbf{Z}_x, \mathbf{Y}_x]\}]^{-1} \ \geq \ 1, \tag{2.11}$$

under the assumption that

$$\|\mathbf{\Delta}_x\|_\infty < 1. \tag{2.12}$$

The definition of complementary stability follows directly from the robust stability condition which in this thesis makes use of the structured singular value, more precisely the mixed-μ theorem. The definition thus states that a robot interacting with any port impedances Z_o and Z_e within the dynamics sets defined by (2.4) and (2.5) is complementary stable for $\|\mathbf{\Delta}_x\|_\infty \ < \ 1$ *iff* $\sup_{\omega\in\mathbb{R}} \mu_{\mathbf{\Gamma}}(\mathbf{M}_x) \ \leq \ 1$.

This analysis leads to a wider range of controllers, including passive and nonpassive ones, and allows to further improve the performance of bilateral systems.

2.5 Optimization Criteria

Now that the bilateral stability condition is established, a performance index is needed. In Buerger and Hogan [2007], a cost function that corresponds to the difference between the robot impedance and a desired impedance is proposed. This choice is adequate for a unilateral interaction, but for a bilateral interaction where two impedances are present, this performance index is ineffective. It is therefore interesting to consider different options.

2.5.1 Performance Indices

For bilateral systems, the first performance criterion to consider is undoubtedly the transparency (Lawrence [1993]). This criterion evaluates the correspondence between the environment impedance and the impedance transmitted to the operator, such that a perfect transparency would result into

$$Z_t = Z_e \tag{2.13}$$

where the transmitted impedance Z_t is defined as $F_o = Z_t V_o$. It is important to recall here that the optimization is performed on each Cartesian motion individually, such that each variable in this section and the next one represents a single component and is taken from the matrix diagonal. Using (2.2) and (2.3), one may find the relationship with the manipulator port admittances that follows

$$Z_t = \frac{F_o}{V_o} = \frac{1}{Y_{oo} + \frac{Y_{oe}Y_{eo}}{\frac{1}{Z_e}+Y_{ee}}}. \tag{2.14}$$

Also, if a steady-state is assumed, such that $V_o = V_e$, the amplification factor, β, can be obtained with the port function (2.3) as follows

$$\frac{F_e}{F_o} = \frac{Y_{oo} - Y_{eo}}{Y_{oe} - Y_{ee}} = \beta. \tag{2.15}$$

Therefore, using equations (2.14) and (2.15) it is possible to find the conditions that lead to equation (2.13), i.e., perfect transparency, which yields

$$Y_{oo} = \beta Y_{oe}, \tag{2.16}$$

$$Y_{eo} = \beta Y_{ee}, \tag{2.17}$$

$$\frac{1}{Y_{oo}} = \frac{1}{Y_{ee}} = 0. \tag{2.18}$$

These conditions also lead to a first optimization criterion related to the amplification capability of the system in steady-state, also known as kinematic correspondence (Hashtrudi-Zaad and Salcudean [2002], Chang and Kim [2012]). Equation (2.15) may be numerically unstable knowing that a transparent system would require that $Y_{ee} = Y_{oe}$. It is thus preferable to use equation (2.16) or (2.17) to assess the amplification performance. This assumption provides a very close estimate of equation (2.15) along with more stable computations.

The measure of the amplification turns out to be a relevant criterion for the optimization process, but it still excludes the environment impedance. A transparency index is therefore necessary to evaluate the transmission capability. The Z-width principle proposed in Colgate and Brown [1994] provides a certain estimation of the dynamic range of the transmitted impedance and bears the following equations :

$$Z_{tmin} = Z_t|_{Z_e=0} = \frac{1}{Y_{oo}}, \tag{2.19}$$

$$Z_{tmax} = Z_t|_{Z_e\to\infty} = \frac{1}{Y_{oo} - \frac{Y_{oe}Y_{eo}}{Y_{ee}}}, \tag{2.20}$$

$$Z_{twidth} = Z_{tmin} - Z_{tmax}. \tag{2.21}$$

A perfectly transparent system would obviously lead to $|Z_{twidth}| \to \infty$. The Z-width holding the two extreme cases of impedance, namely free motion and clamped interactions, respectively depicted by equations (2.19) and (2.20), attempts to include the whole impedance spectrum. However, depending on the situation, including both extreme conditions might not be necessary. Here, the interaction of interest implies a contact with a high impedance environment. Equation (2.20) should thus be sufficient to assess the transparency performance and is thereby proposed as a second optimization criterion.

Although the above two criteria cover major performance aspects of bilateral interactions, a third criterion focusing more on the transient response would greatly improve the optimization process. Therefore, the integral of the time-weighted absolute error (ITAE), commonly used in servo design (Martins [2005]), is also included. This performance index evaluates the system response to a unit step input and is defined as

$$ITAE = \int_0^\infty t|\epsilon|dt \tag{2.22}$$

where t is the time variable and ϵ is the error between the output and the set point. In other words, this index provides a cost related to the settling time and the overshoot of a transient response. The ITAE cost is thus computed on the manipulator admittance Y_{eo} which relates the operator input force and the output environment velocity. However, it could also be used on any manipulator function and would still hold the same comparative meaning.

To summarize, all three optimization criteria are presented here with their related cost :

1. Amplifcation index, noted C_β

$$C_\beta = \frac{\sum_{i=1}^{n} |\beta - \frac{|Y_{eo}(j\omega_i),|}{|Y_{ee}(j\omega_i)|}|}{n}, \tag{2.23}$$

2. Transparency index, noted C_T

$$C_T = \frac{\sum_{i=1}^{n} ||Y_{oo}(j\omega_i)| - \frac{|Y_{oe}(j\omega_i)||Y_{eo}(j\omega_i)|}{|Y_{ee}(j\omega_i)|}|}{n}, \tag{2.24}$$

3. ITAE index, noted C_I

$$C_I = \int_0^\tau t|\epsilon|dt \tag{2.25}$$

where n is the total number of frequencies, ω_i, evaluated in the desired frequency range, τ is the upper bound on the desired time range, and j is the imaginary unit ($j = \sqrt{-1}$). Here, τ is equal to 1 second in order to ensures that the steady state can be reached, and the frequency range $\omega_i \in [10^{-2}, 10^2]$ rad/s (or [0.0016, 16] Hz) is used in order to include the typical human interaction frequencies. Indeed, a human physical input has a typical responsiveness of about 5 Hz, and can reach in some cases a maximum responsiveness around $10 - 12$ Hz, as demonstrated in Brooks [1990] and Jones [2000]. A frequency range upper bound three times the typical human responsiveness is thus considered as sufficient for the optimization.

2.5.2 Controller Comparison

The next step to evaluate the optimal parameter values for typical unilateral controller structures is to devise an optimization strategy involving the aforementioned performance indices and thereby, achieving an optimal controller. Different controllers and different parameter sets should be tested in order to obtain a more complete cluster of potential outcomes. A simple way to optimize the set of parameters of a pre-defined controller structure is to minimize the sum of the normalized performance costs that are complementary stable, i.e.,

$$C = \mathbf{w}^T \, [\, \bar{C}_\beta, \bar{C}_T, \bar{C}_I \,]^T \tag{2.26}$$

where C is the global cost associated with a given set of parameters and $\mathbf{w}^T = [w_\beta, w_T, w_I]$ is the weighting vector used to reflect the priority level of each normalized cost $\bar{C}_\beta$, $\bar{C}_T$, and $\bar{C}_I$. The unity-based normalization is calculated over all the sets of parameters evaluated, with the minimum and maximum costs of each index computed as follows

$$C_{xmin} = min|\mathbf{C}_x| \tag{2.27}$$

$$C_{xmax} = max|\mathbf{C}_x| \tag{2.28}$$

where $\mathbf{C}_x$ represents a matrix including all computed costs for each performance index with the index x referring to the different indices, namely $x \in \{\beta, T, I\}$.

An example is provided for an admittance control, also known as lowpass control, and is defined by the following general transfer function :

$$G_{adm} = \frac{\beta_x}{m_v s + c_v} = \frac{\frac{\beta_x}{c_v}}{\frac{m_v}{c_v} s + 1} \tag{2.29}$$

where G_{adm} is related to the diagonal elements of $\mathbf{G}_o$ and $\mathbf{G}_e$ of Fig. 2.3, m_v and c_v are respectively the virtual inertia and virtual damping, and β_x is a parameter that defines the desired force amplification between the operator (β_o for $\mathbf{G}_o$) and the environment (β_e for $\mathbf{G}_e$).

Here, the human force is amplified by a factor of 5, thereby, $\beta_o = 1$ and $\beta_e = 1/5$. The robot manipulator dynamics used for the optimization example of the bilateral interaction is that of a seven-dof Kuka LWR (Albu-Schäffer et al. [2007]) with two six-axis force/torque sensors, one at the end-effector for the environment input and another one on the fourth link, just upstream from the spherical wrist, for the operator input. The experimental set-up is shown in Fig. 2.6.

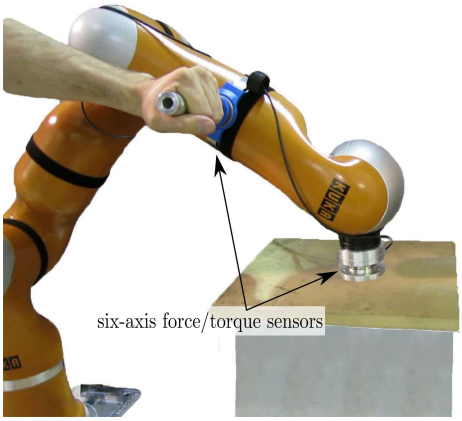

FIGURE 2.6 – The seven-dof Kuka LWR with two six-dof force/torque sensors used for the experimentation and optimization.

The next step, after establishing the control loop and robot dynamics, is to define the human and environment uncertain dynamics for the computation of the complementary stability. An appropriate choice for the human uncertain impedance parameters is given in Buerger and Hogan [2007], namely $m_o \in [0.1, 4.1]$ kg, $c_o \in [0.01, 41]$ Ns/m, and $k_o \in [1, 401]$ N/m. The environment uncertain impedance is slightly more complex to estimate. Based on the experiments performed by the authors, it is believed that the range of parameters used in Peer and Buss [2008] is in fact too soft. The minimum and maximum stiffness have thus been increased to represent a stiffer environment and exclude free motion and soft interactions. In other words, only bilateral interactions with stiff environments are considered for the force amplification control optimization. The damping has also been increased. Therefore, the environment uncertain impedance parameters are given by $m_e \in [0.1, 1]$ kg, $c_e \in [50, 300]$ Ns/m, and $k_e \in [4 \times 10^4, 2.6 \times 10^5]$ N/m. Thereafter, a certain robot configuration is assumed which is the static position depicted in Fig. 2.13. Then, the complementary stability is verified for a range of potential controller parameters $(\beta_o/c_v, m_v/c_v)$, and can be visualized in Fig. 2.7 for the z-direction, where a robust stability margin below one is considered unstable (represented in white). With the stable parameters confirmed, the costs can be computed. The results for the three intermediate performance costs are shown in Fig. 2.8, 2.9 and 2.10.

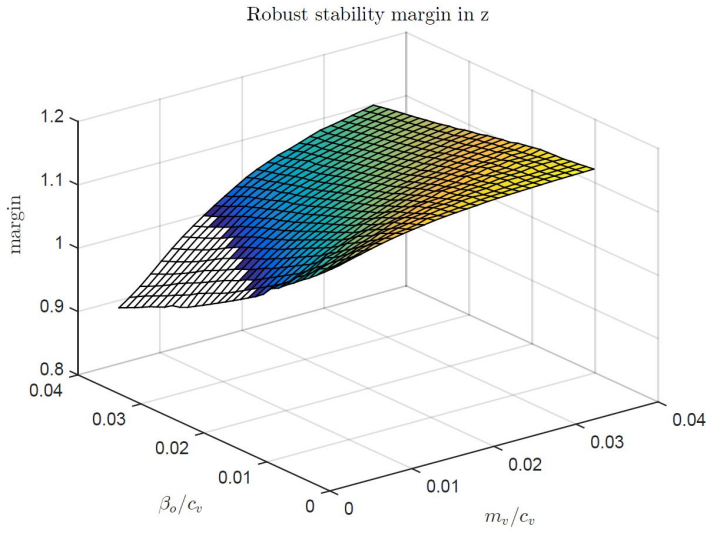

FIGURE 2.7 – Robust stability margin which establishes whether the system is complementary stable for the z-direction. A margin ≥ 1 leads to a robustly stable interaction.

It is reassuring to see that classical servo design behaviours are observed. Indeed, the amplification index, which assesses the tracking performance, tends to give better results mostly for high DC gain, β_o/c_v. On the other hand, the ITAE index, assessing the time response, tends to be much more influenced by a low time constant, m_v/c_v. Meanwhile, the transparency index yields a lower cost for lower DC gains as the infinite environment impedance is transmitted on a larger bandwidth. The global performance cost is also depicted in Fig. 2.11 and reveals that the lowest possible time constant, limited by the robot hardware, leads to the optimal performance.

However, in order to compare different controller dynamics, including distinct sets of parameters, the approach has to be slightly modified. Indeed, each normalized performance index in (2.26) must be computed in terms of the minimum and maximum values of all the different controllers. This way, they are set on the same baseline and their summation results in a meaningful global cost C. For instance, if n different controllers are to be studied, the minimum and maximum costs for the computation of each unity-based normalized index becomes

$$C_{xmin} = min(|\mathbf{C}_{x1}|, |\mathbf{C}_{x2}|, ..., |\mathbf{C}_{xn}|) \tag{2.30}$$

$$C_{xmax} = max(|\mathbf{C}_{x1}|, |\mathbf{C}_{x2}|, ..., |\mathbf{C}_{xn}|) \tag{2.31}$$

where the index x is, again, referring to the different indices (β, T, or I).

Using this approach, a PI controller, an admittance controller and a lead/lag controller have been compared. The PI controller is known to yield good results for bilateral systems and is

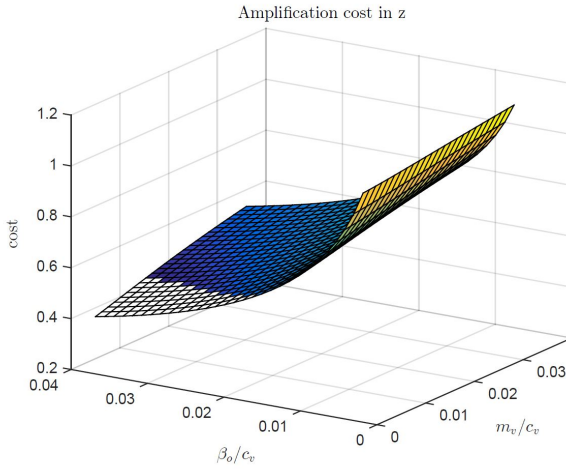

FIGURE 2.8 – Cost related to the amplification index in the z-direction. A low amplification cost leads to better tracking performance.

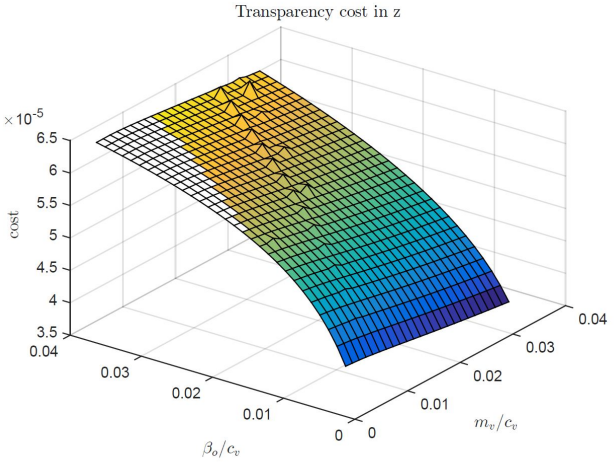

FIGURE 2.9 – Cost related to the transparency index for the z-direction. A low transparency cost leads to better environment impedance transmission.

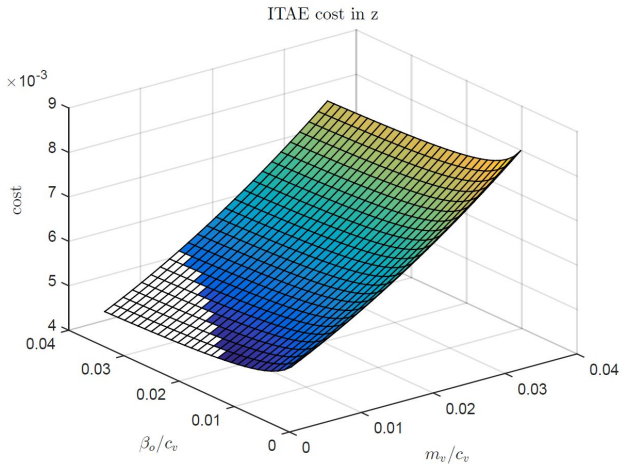

FIGURE 2.10 – Cost related to the ITAE index for the z-direction. A low ITAE cost leads to faster time response.

often used due to its simplicity. By contrast, the admittance controller is known for its effective haptic rendering that is highly appreciated for unilateral human-robot interaction, but is often forsaken for bilateral interaction due to its poor performance for stiff environments (Ott et al. [2010]). Lead and lag controllers are hardly used in this field of robotics but the positive results presented in Buerger and Hogan [2007] make them interesting controllers to evaluate, even if a qualitative study would be necessary to assess the intuitiveness of the resulting unilateral interaction. The following lead/lag controller form has been used to assess the optimal lead

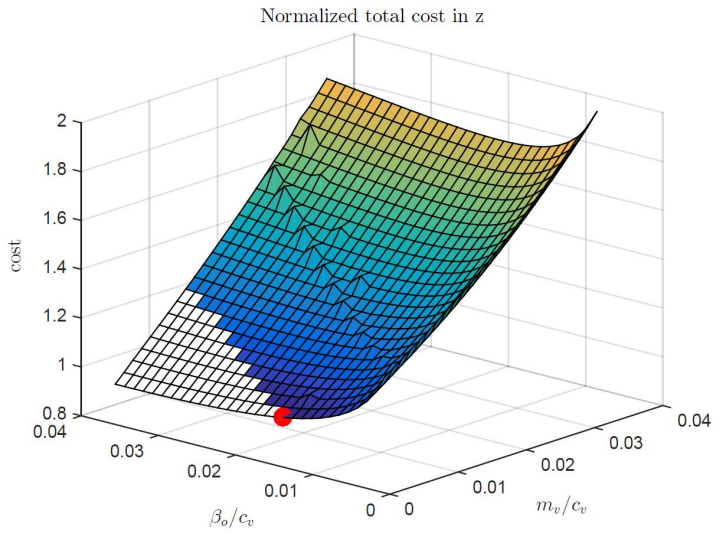

FIGURE 2.11 – Global cost of the normalized performance indices in the z-direction with $\mathbf{w}^T = [1, 1, 1]$. The red dot represents the optimal set of parameters

or lag controller for a bilateral amplification task :

$$G_{ll} = K_{ll}\frac{s+z}{s+p}. \tag{2.32}$$

The gain K_{ll}, the zero frequency z and the pole frequency p are therefore the three parameters to optimize. The comparative results, presented in table 2.1, demonstrate overall that the admittance controller leads to better results than the PI, even if the latter yields a slightly better performance for the transparency index. The main difference comes from the ITAE index and is depicted in Fig. 2.12 for a 5 Hz operator force amplification. This pursuit example, performed on the experimental set-up shown in Fig. 2.6 with the optimal PI and admittance controllers, clearly demonstrates the faster transient response of the admittance. However, it is found that a lag compensator can analytically outperform the admittance. It thus reveals that the lead/lag controller form should also be viewed as a viable type of compensation for bilateral interactions. Although the lag compensator presents better performances it would be interesting, with the results at hand, to prove that an admittance control can be highly efficient in a stiff multi-dof bilateral interaction context. This could encourage the use of such a controller for all types of bilateral tasks, not only for soft contacts. Therefore, further optimizations related to the multi-dof nature of the Kuka-LWR have been carried out with the admittance controller.

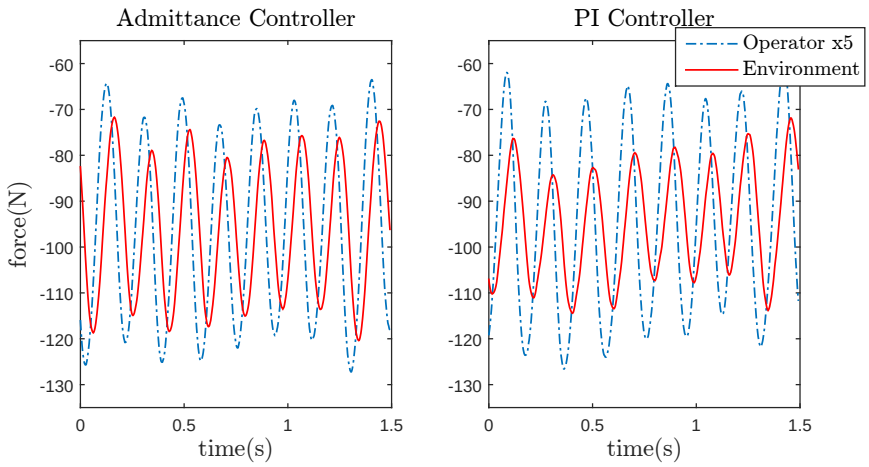

FIGURE 2.12 – High-frequency amplification pursuit for an admittance and a PI controller. The operator force is amplified 5 times for comparison purposes.

TABLE 2.1 – Best relative global costs of different control schemes and their corresponding criteria.

	ITAE	Transparency	Amplification	Global
PI	0.0451	5.636×10^{-5}	0.6338	0.3527
Admittance	0.0051	6.168×10^{-5}	0.4360	0.1606
Lead/lag	8.730×10^{-4}	6.452×10^{-5}	0.3147	0.0746

2.6 Multi-DoF Optimization

A major control issue with multi-dof robots is that their dynamics are configuration dependent. In order to assess the optimal controller for a multi-dof robot amplification, it is thus necessary to find a variable that describes the changes in dynamics related to the different joint configurations. Identifying the optimal controller parameters related to such a variable would lead to a regulator that is optimal for all configurations of the manipulator. An interesting approach to this problem is the joint stiffness matrix mapping the joint torques, $\boldsymbol{\tau}$, to the joint displacements, $\delta\theta$, (Salisbury [1980]), such that

$$\boldsymbol{\tau} = \mathbf{K}_\theta \delta\boldsymbol{\theta} \tag{2.33}$$

where $\mathbf{K}_\theta$ is the joint stiffness matrix. Considering that the control is computed in the Cartesian space, a joint-dependent variable that maps the relationship between the end-effector generalized displacements, $\delta\mathbf{x}$, and forces, $\mathbf{f}$, is thus more appropriate. Therefore, with the use of the manipulator Jacobian, enabling the following relationships :

$$\boldsymbol{\tau} = \mathbf{J}^T\mathbf{f}, \tag{2.34}$$

$$\mathbf{J}\delta\boldsymbol{\theta} = \delta\mathbf{x}, \tag{2.35}$$

it becomes straightforward with (2.33) to find the coveted relationship, such that

$$\delta \mathbf{x} = (\mathbf{J}\mathbf{K}_\theta{}^{-1}\mathbf{J}^T)\mathbf{f} \tag{2.36}$$

where $(\mathbf{J}\mathbf{K}_\theta{}^{-1}\mathbf{J}^T)$ is referred to as the Cartesian compliance matrix. Here, the joint stiffness matrix is diagonal and all joints are assumed to have the same stiffness, thus $\mathbf{K}_\theta = diag\{1, 1, 1, 1, 1, 1\}$ [1]. Equation (2.36) is a direct relationship between the Cartesian forces and the Cartesian displacements at the end-effector using only the Jacobian transformation — which is an index of the joint configuration. In other words, the Cartesian compliance matrix introduces a measurement of the variation of the end-effector dynamics related to the manipulator configuration, and may be used to find the optimal controller parameters.

2.6.1 Continuous Gain Scheduling

The next step is to perform the optimization on a set of different configurations generating different compliance values. Therefore, the seven-dof Kuka LWR showed in Fig. 2.6 has been used to conduct the current analysis and the corresponding experimentation. The chosen configuration set includes 20 consecutive end-effector positions that produce a horizontal displacement along the robot's Cartesian x-axis, as depicted in Fig. 2.13.

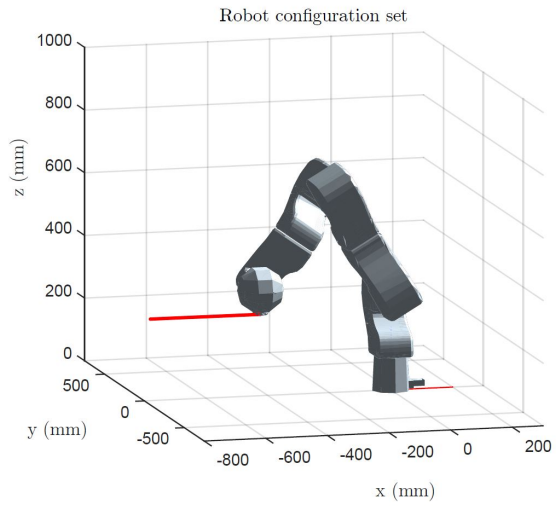

FIGURE 2.13 – End-effector horizontal displacement that generates the manipulator configuration set used for the optimization analysis.

The complementary stability as well as the optimization are then evaluated for each configuration. Afterwards, the different gains, β_o/c_v, and time constants, m_v/c_v, obtained with the algorithm are plotted with their related compliance in Fig. 2.14.

1. The joint stiffness may be set arbitrarily and will affect all indices equally

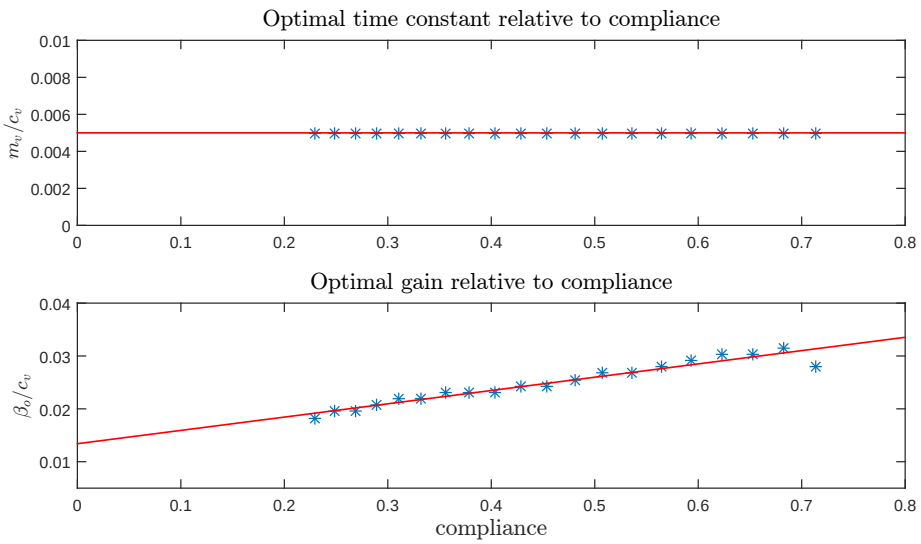

FIGURE 2.14 – Optimal m_v/c_v and β_o/c_v values relative to the manipulator compliance along the z-axis, and therefore the robot configuration.

Here, only the relationship with the axis including the wider range of compliance values along the evaluated trajectory is shown, i.e., the z-axis. As expected, regardless of the configuration, the optimal m_v/c_v parameter value is the lowest frequency limit that the hardware can support. On the other hand, the optimal β_o/c_v parameter value appears to change linearly with the manipulator compliance.

In other words, the stiffer the configuration becomes, the more the gain needs to be scaled down. This result is rather intuitive and goes along with the typical effect of a DC gain variation for servo design. This interesting result leads to a simple gain scheduling law that solves the dynamics issue with multi-dof manipulators, and thereby yields an optimal bilateral amplification for all configurations. It is important to note that this relationship is optimal for the specific range of impedance dynamics (impedance of the human operator and of the stiff environment) evaluated with the robust stability analysis. For instance, using a lower bound on the environment stiffness would shift down the relationship between the gain and the compliance.

2.6.2 Impact Tests

The coupled stability and the performance were tested with manually generated impact motions on three different surfaces that were respectively below, inside, and above the range of stiff environment k_e evaluated in the algorithm. The objective is to verify whether the parameters found can work outside of the optimization set. These surfaces are : a stiff spring

(stiffness = 5.12×10^3 N/m), a rubber stopper (stiffness = 9.15×10^4 N/m), and a 100×100 mm aluminum square tube (stiffness >> $k_{e\,max}$). The operator produced a 20 N impact that was amplified five times to generate an output of 100 N on the environment. During this amplification, unilateral motions in the other Cartesian directions were controlled using an admittance controller but with different parameter values than the one used for bilateral interactions. The results for a *stiff* manipulator configuration with a compliance around 0.2 m/N are shown in Fig. 2.15 for three distinct sets of controller parameters.

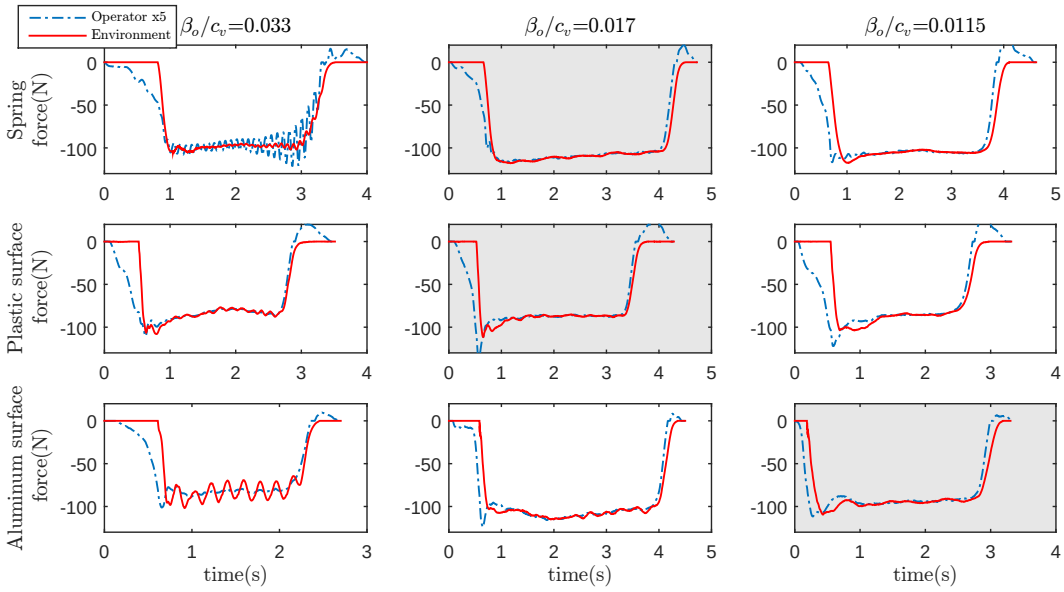

FIGURE 2.15 – Impact tests on three different environments, namely a spring, a plastic surface, and an aluminum surface, for three distinct values of parameter β_o/c_v of the admittance controller. The operator force is amplified 5 times for comparison purposes. The best response for each surface is identified by a shaded background.

From the linear gain scheduling presented in Fig. 2.14, the optimal β_o/c_v parameter value should be between 0.015 and 0.02 for an environment stiffness between 4×10^4 and 2.6×10^5 N/m. Thereby, gains of 0.0115, 0.017, and 0.033 have been chosen to study the optimization outputs. Parameter m_c/c_v is kept constant at 0.005 for all tests.

Any oscillation or vibration felt by the operator was sorted out by the performance criteria. Indeed, undesirable oscillations appear when admittance regulator gains are too high for a specific manipulator configuration as it is depicted in Fig. 2.15 for $\beta_o/c_v = 0.033$. Both the rubber and the aluminum surfaces induce instability but the aluminum surface, being stiffer, generates larger oscillations. The interaction with the spring is also clearly unstable for this gain value, but in that case the system could not keep up with the amplified force on the

environment without creating a divergent force on the operator. For the optimal gain value $\beta_o/c_v = 0.017$, the impact on the aluminum surface does not produce a perfectly stable interaction, unlike the impacts on the rubber surface and the spring that lead to fast and precise responses. The smallest gain value $\beta_o/c_v = 0.0115$ suits better the harder surface but it is slightly slower, as it can easily be seen for the transition phases of the spring and rubber amplifications. Indeed, a gain lower than the optimal value slows down the response and in extreme cases could lead to a stiction effect when quick pull-offs are performed. This effect is depicted in Fig. 2.16 for a 0.15 second stiction which required an additional 4 N to rapidly move the end-effector. However, that necessary additional force remained unfelt by the operator.

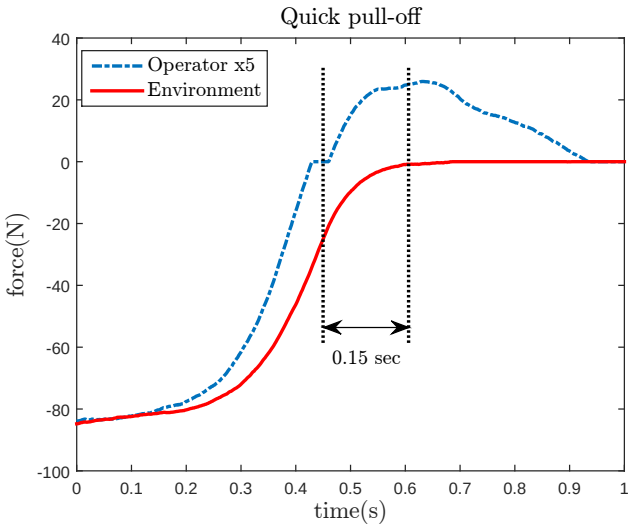

FIGURE 2.16 – Demonstration of an unfelt small stiction effect for a quick pull-off.

These experiments reveal that the optimization technique is thus effective for the environment (rubber stopper) that is contained within the range of uncertainties previously evaluated. It also demonstrates that it can accommodate different environments that are outside of this range (softer or stiffer) while providing reasonably good results. In summary, the optimization algorithm developed here allows to find a controller that yields extremely high performance while remaining robustly stable for pre-defined interaction environments for a mutli-dof robotic manipulator whose dynamics vary greatly with the configuration.

2.7 Video Demonstration

The accompanying video, featuring the seven-dof Kuka LWR, demonstrates the effectiveness of the control gain scheduling resulting from the optimization (*Chap2_Control_Opt.mp4*).

The first part consists of a horizontal amplification combined with a vertical displacement. This human-robot interaction shows the variation of the gain β_o/c_v as a function of the manipulator's Cartesian compliance in the direction normal to the interaction surface. The second part presents the impact test performed in order to evaluate the optimal controller previously found with the optimization algorithm. Unstable and stable behaviour, using respectively a high gain and a gain scheduling, are demonstrated with a spring and an aluminum surface. The video is available at

http://robot.gmc.ulaval.ca/publications/these-de-doctorat

2.8 Conclusion

In this chapter, a procedure to assess the complementary stability of a bilateral system was presented. The specific case of force amplification with a multi-dof manipulator was studied in order to optimize the parameter values of well-known controller structures used for unilateral interactions. The optimization technique is based on three distinct performance indices, namely the amplification, the transparency, and the ITAE. This approach allows to compare different control architectures. This method is also a powerful tool to address control issues with varying dynamics. However, it is required to have a configuration-related variable, which is defined here as the Cartesian manipulator compliance matrix. A relationship between the compliance and the different control parameters can then be obtained. The impact tests carried out with a seven-dof Kuka LWR demonstrated the high performance and robust stability achieved with the optimal control parameters.

The main focus of the chapter was on force amplification, but a interesting future study with this optimization approach would be to assess the optimal position of the operator's handle on the manipulator in order to obtain the best transparency. The optimal amplification parameters for the Cartesian torques could also be evaluated since only the forces have been studied up to now. Moreover, it would be interesting to test different configuration-related variables such as the Conservative Congruence Transformation (CCT) (Li and Kao [2003]). Although it has been demonstrated that the controller optimization algorithm developed here is an adequate tool for a single robot multi-dof bilateral amplification, it is important to note that the general framework presented can be extended to various unilateral or bilateral interactions, as well as haptics. Since little work as been done on the optimal performance related to the robot configuration, it is also interesting to investigate whether the gain scheduling resulting from the optimization could provide a means of obtaining the best multi-dof performance regardless of the robot varying dynamics, for all kinds of manipulators.

2.9 Appendix

2.9.1 Compliant Manipulator and Controller Dynamics

Remark : All variables used in the appendix are defined in the following figure captions. The values of the model parameters used for the Kuka LWR are determined from the information given in Albu-Schäffer et al. [2007] and are listed online at

robot.gmc.ulaval.ca/fileadmin/share/kuka_parameters.pdf

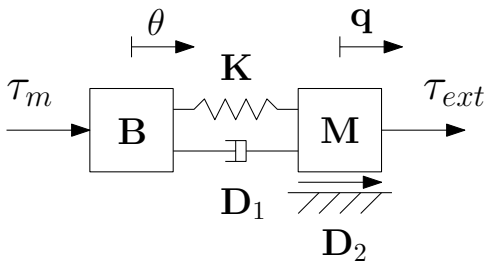

FIGURE 2.17 – Schematic representation of a compliant robotic manipulator. The actuators inertia matrix $\mathbf{B}$ and the links inertia matrix $\mathbf{M}$ are connected by the stiffness matrix $\mathbf{K}$ and the damping matrix $\mathbf{D}_1$. The centripetal and Coriolis force matrix $\mathbf{D}_2$ is acting on the links. The actuators torque vector and the external torque vector are respectively represented by $\boldsymbol{\tau}_m$ and $\boldsymbol{\tau}_{ext}$, while $\boldsymbol{\theta}$ and $\mathbf{q}$ are the vectors of joint coordinates associated with the actuators and the links.

The dynamic model of the Kuka LWR is based on the elastic joint model defined in Spong [1987] and can be derived from the schematic representation given in Fig. 2.17, as follows

$$\mathbf{M}(\mathbf{q})\ddot{\mathbf{q}} + \mathbf{D}_2(\mathbf{q},\dot{\mathbf{q}})\dot{\mathbf{q}} = \mathbf{K}(\boldsymbol{\theta} - \mathbf{q}) + \mathbf{D}_1(\dot{\boldsymbol{\theta}} - \dot{\mathbf{q}}) - \boldsymbol{\tau}_{ext}, \tag{2.37}$$

$$\mathbf{B}\ddot{\boldsymbol{\theta}} + \mathbf{K}(\boldsymbol{\theta} - \mathbf{q}) + \mathbf{D}_1(\dot{\boldsymbol{\theta}} - \dot{\mathbf{q}}) = \boldsymbol{\tau}_m \tag{2.38}$$

where the external torque vector $\boldsymbol{\tau}_{ext}$ includes the operator and the environment forces and yields

$$\boldsymbol{\tau}_{ext} = \mathbf{J}_o^T\mathbf{F}_o - \mathbf{J}_e^T\mathbf{F}_e. \tag{2.39}$$

The friction torques are neglected in the dynamics equations and the gravity torques can be removed thanks to the gravity compensation included in the Kuka's joint state feedback controller given in Albu-Schäffer et al. [2007]. Therefore, the position control law without the gravity vector yields

$$\boldsymbol{\tau}_m = -\mathbf{K}_P(\boldsymbol{\theta} - \boldsymbol{\theta}_d) - \mathbf{K}_D\dot{\boldsymbol{\theta}} - \mathbf{K}_T\boldsymbol{\tau} - \mathbf{K}_S\dot{\boldsymbol{\tau}} \tag{2.40}$$

where the spring torque vector $\boldsymbol{\tau}$ is defined by

$$\boldsymbol{\tau} = \mathbf{K}(\boldsymbol{\theta} - \mathbf{q}), \tag{2.41}$$

but where the desired motor position vector is defined with the gravity vector $\mathbf{g}(\mathbf{q}_d)$ and yields

$$\boldsymbol{\theta}_d = \mathbf{q}_d + \mathbf{K}^{-1}\mathbf{g}(\mathbf{q}_d). \tag{2.42}$$

However, considering that the gravity vector remains nearly constant for an amplification task it is possible to say, for the desired motor velocity vector, that $\dot{\boldsymbol{\theta}}_d \approx \dot{\boldsymbol{q}}_d$. Note that this assumption is taken because the outer control of the manipulator relates the external forces to desired velocities.

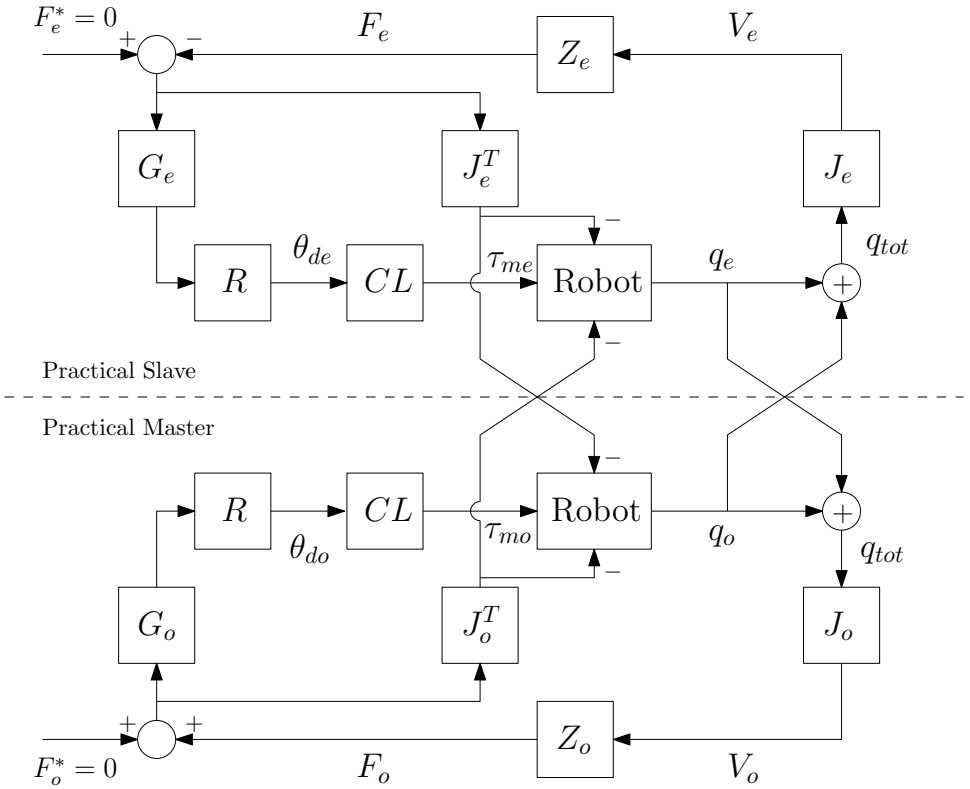

FIGURE 2.18 – Extended block diagram of the bilateral interaction for a practical slave and a practical master. In reality there is only one manipulator, thereby both practical manipulators have the same redundancy resolution $\mathbf{R}$, control model CL, robot model *Robot*, and the same total joint position output vector $\mathbf{q}_{tot}$. However, $\mathbf{Z}_o$, $\mathbf{V}_o$, $\mathbf{F}_o$, $\mathbf{F}_o^*$, $\mathbf{G}_o$, $\mathbf{J}_o$, $\boldsymbol{\theta}_{do}$, $\boldsymbol{\tau}_{mo}$, and $\mathbf{q}_o$ are respectively, the human operator impedance matrix and velocity vector, the operator force vector that is applied on the practical master, the exogenous operator force input vector, the operator regulator matrix, the operator Jacobian matrix, the operator desired motor position vector, the operator motor torque command vector, and the operator joint position vector while $\mathbf{Z}_e$, $\mathbf{V}_e$, $\mathbf{F}_e$, $\mathbf{F}_e^*$, $\mathbf{G}_e$, $\mathbf{J}_e$, $\boldsymbol{\theta}_{de}$, $\boldsymbol{\tau}_{me}$, and $\mathbf{q}_e$ are defined similarly but for the environment.

In order to use the teleoperation analysis tools, the control architecture is divided in two virtually different manipulators, namely the practical master interacting with the human operator and the practical slave interacting with the environment. Each practical manipulator has its own torque command, which is $\boldsymbol{\tau}_{mo}$ for the practical master and $\boldsymbol{\tau}_{me}$ for the practical slave. The corresponding extended control architecture is shown in Fig. 2.18 and the following mathematical development evaluates the output position of each practical manipulator, namely $\mathbf{q}_o$ and $\mathbf{q}_e$. According to the block diagram, the desired motor position vector is thus

given by

$$\boldsymbol{\theta}_{dx} = \mathbf{R}\mathbf{G}_x\mathbf{F}_x \tag{2.43}$$

where $\boldsymbol{\theta}_{dx}$, $\mathbf{G}_x$, and $\mathbf{F}_x$ can be $\boldsymbol{\theta}_{do}$, $\mathbf{G}_o$, and $\mathbf{F}_o$, or $\boldsymbol{\theta}_{de}$, $\mathbf{G}_e$, and $\mathbf{F}_e$. It is recalled that the redundancy resolution $\mathbf{R}$ includes an integrator.

Linearising equation (2.37) with $\mathbf{M}$ and $\mathbf{D}_2$ as constants allows to express the equations of dynamics in the Laplace domain as follows

$$(\mathbf{M}s^2 + \mathbf{D}_2 s + \mathbf{D}_1 s + \mathbf{K})\mathbf{q}_x = (\mathbf{D}_1 s + \mathbf{K})\boldsymbol{\theta}_x - \boldsymbol{\tau}_{ext}, \tag{2.44}$$

$$(\mathbf{B}s^2 + \mathbf{D}_1 s + \mathbf{K})\boldsymbol{\theta}_x = (\mathbf{D}_1 s + \mathbf{K})\mathbf{q}_x + \boldsymbol{\tau}_{mx} \tag{2.45}$$

and the control law (2.40) with equations (2.41) and (2.43) leads to

$$\boldsymbol{\tau}_{mx} = \mathbf{G}_1\boldsymbol{\theta}_x + \mathbf{G}_2\mathbf{q}_x + \mathbf{G}_{fx}\mathbf{F}_x \tag{2.46}$$

where

$$G_1 = -(\mathbf{K}_D + \mathbf{K}_S\mathbf{K})s - \mathbf{K}_P - \mathbf{K}_T\mathbf{K}, \tag{2.47}$$

$$G_2 = (\mathbf{K}_S\mathbf{K})s + \mathbf{K}_T\mathbf{K}, \tag{2.48}$$

$$G_{fx} = \mathbf{K}_P\mathbf{R}\mathbf{G}_x, \tag{2.49}$$

and $\boldsymbol{\tau}_{mx}$, $\boldsymbol{\theta}_x$, and $\mathbf{q}_x$ can be $\boldsymbol{\tau}_{mo}$, $\boldsymbol{\theta}_o$, and $\mathbf{q}_o$ or $\boldsymbol{\tau}_{me}$, $\boldsymbol{\theta}_e$, and $\mathbf{q}_e$. Then, in order to close the loop on one practical manipulator, equation (2.46) is substituted into equation (2.45) as follows

$$\mathbf{A}_1\boldsymbol{\theta}_x = \mathbf{A}_4\mathbf{q}_x + \mathbf{G}_{fx}\mathbf{F}_x \tag{2.50}$$

where

$$\mathbf{A}_1 = \mathbf{B}s^2 + \mathbf{D}_1 s + \mathbf{K} - \mathbf{G}_1, \tag{2.51}$$

$$\mathbf{A}_4 = \mathbf{D}_1 s + \mathbf{K} + \mathbf{G}_2, \tag{2.52}$$

and equation (2.50) can be solved for $\boldsymbol{\theta}$ such that

$$\boldsymbol{\theta}_x = \mathbf{A}_1^{-1}[\mathbf{A}_4\mathbf{q}_x + \mathbf{G}_{fx}\mathbf{F}_x]. \tag{2.53}$$

Afterwards, equations (2.53) and (2.39) are substituted into (2.44), which yields

$$\mathbf{A}_2\mathbf{q}_x + \mathbf{J}_o^T\mathbf{F}_o - \mathbf{J}_e^T\mathbf{F}_e = \mathbf{A}_3\mathbf{A}_1^{-1}[\mathbf{A}_4\mathbf{q}_x + \mathbf{G}_{fx}\mathbf{F}_x] \tag{2.54}$$

where

$$\mathbf{A}_2 = \mathbf{M}s^2 + (\mathbf{D}_1 + \mathbf{D}_2)s + \mathbf{K}, \tag{2.55}$$

$$\mathbf{A}_3 = \mathbf{D}_1 s + \mathbf{K}. \tag{2.56}$$

Equation (2.54) can then be solved for $\mathbf{q}_x$, yielding

$$\mathbf{q}_x = [\mathbf{A}_1\mathbf{A}_3^{-1}\mathbf{A}_2 - \mathbf{A}_4]^{-1}[\mathbf{G}_{fx}\mathbf{F}_x - \mathbf{A}_1\mathbf{A}_3^{-1}\mathbf{J}_o^T\mathbf{F}_o + \mathbf{A}_1\mathbf{A}_3^{-1}\mathbf{J}_e^T\mathbf{F}_e]. \tag{2.57}$$

For each practical manipulator, the output position is thus defined as follows

$$\mathbf{q}_o = [\mathbf{A}_1\mathbf{A}_3^{-1}\mathbf{A}_2 - \mathbf{A}_4]^{-1}[(\mathbf{G}_o - \mathbf{A}_1\mathbf{A}_3^{-1}\mathbf{J}_o^T)\mathbf{F}_o + \mathbf{A}_1\mathbf{A}_3^{-1}\mathbf{J}_e^T\mathbf{F}_e] \tag{2.58}$$

and

$$\mathbf{q}_e = [\mathbf{A}_1\mathbf{A}_3^{-1}\mathbf{A}_2 - \mathbf{A}_4]^{-1}[-(\mathbf{G}_e - \mathbf{A}_1\mathbf{A}_3^{-1}\mathbf{J}_e^T)\mathbf{F}_e - \mathbf{A}_1\mathbf{A}_3^{-1}\mathbf{J}_o^T\mathbf{F}_o], \tag{2.59}$$

but considering that the master and slave are represented by the same robot, the real manipulator displacement is rather $\mathbf{q}_{tot} = \mathbf{q}_o + \mathbf{q}_e$ and yields

$$\mathbf{q}_{tot} = [\mathbf{A}_1\mathbf{A}_3^{-1}\mathbf{A}_2 - \mathbf{A}_4]^{-1}[(\mathbf{G}_o - 2\mathbf{A}_1\mathbf{A}_3^{-1}\mathbf{J}_o^T)\mathbf{F}_o - (\mathbf{G}_e - 2\mathbf{A}_1\mathbf{A}_3^{-1}\mathbf{J}_e^T)\mathbf{F}_e]. \tag{2.60}$$

Lastly, in order to obtain the components of the two-port matrix in equation (2.3), equation (2.60) is rewritten such that $\mathbf{q}_{tot} = \mathbf{T}_o\mathbf{F}_o + \mathbf{T}_e(-\mathbf{F}_e)$ where

$$\mathbf{T}_o = [\mathbf{A}_1\mathbf{A}_3^{-1}\mathbf{A}_2 - \mathbf{A}_4]^{-1}(\mathbf{G}_o - 2\mathbf{A}_1\mathbf{A}_3^{-1}\mathbf{J}_o^T), \tag{2.61}$$

$$\mathbf{T}_e = [\mathbf{A}_1\mathbf{A}_3^{-1}\mathbf{A}_2 - \mathbf{A}_4]^{-1}(\mathbf{G}_e - 2\mathbf{A}_1\mathbf{A}_3^{-1}\mathbf{J}_e^T) \tag{2.62}$$

and then, the velocity vectors are expressed as follows

$$\mathbf{V}_o = \mathbf{J}_o\mathbf{T}_o\mathbf{F}_o + \mathbf{J}_o\mathbf{T}_e(-\mathbf{F}_e), \tag{2.63}$$

$$\mathbf{V}_e = \mathbf{J}_e\mathbf{T}_o\mathbf{F}_o + \mathbf{J}_e\mathbf{T}_e(-\mathbf{F}_e) \tag{2.64}$$

which leads to the following two-port matrix

$$\begin{bmatrix} \mathbf{Y}_{oo} & \mathbf{Y}_{oe} \\ \mathbf{Y}_{eo} & \mathbf{Y}_{ee} \end{bmatrix} = \begin{bmatrix} \mathbf{J}_o\mathbf{T}_o & \mathbf{J}_o\mathbf{T}_e \\ \mathbf{J}_e\mathbf{T}_o & \mathbf{J}_e\mathbf{T}_e \end{bmatrix}. \tag{2.65}$$

2.9.2 Considerations and Issues for Robust Stability Analysis

- For this optimization algorithm, μ-analysis is favoured as the robust stability analysis tool, mainly, because of the presence of multiple sources of uncertainty, which can thereby be rearranged into the less conservative structured uncertainty.

- The range of parameter values evaluated is firstly wide and sparse in order to find the boundaries of robust stability and the optimal region to analyze. It is then narrowed around the region of interest so that the precision and computation time are improved.

- The mathematical manipulation performed to obtain the two-port matrix (2.65) can generate state-space systems that contain a large number of state variables. It is therefore required to reduce the systems' order to avoid computation instability and limit the computation time. A balanced realization of $\mathbf{Y}_x$ is thus computed using *Matlab* in order to find the state variables having Hankel singular values smaller than 10^{-7}, which are considered as negligible for the model dynamics. These states can therefore be removed using the function *modred* with the DC gain matching approach. It is critical to check the validity and stability of the reduction before carrying on with the optimization process.

- Another well-known issue with the μ-analysis is the presence of discontinuities in the evaluated set of frequencies. Indeed, the robust stability margin can be erroneous if the destabilizing frequencies are missing in the evaluation range. There are two approaches to alleviate this problem. The first one is to add a complex parametric uncertainty to each real perturbation. This added dynamics improves the conditioning of the robust stability computation (*robuststab* function) but introduces some conservatism in the resulting margin. It is thus important to only add a small amount of complex dynamics. In this chapter, a 5 % conservatism is added with the *complexify* function. The second approach is to densify the frequency range of evaluation in order to obtain more reliable results. In fact, a combination of both approaches yields the best results. Here, uncertain frequency response data model (*ufrd* function) of every feedback interconnection $\mathbf{M}_x - \mathbf{\Delta}_x$ contains 200 frequencies $\in [10^{-2}, 10^{2}]$ rad/s which covers the human interaction range of frequency.